PNAS Nexus, 2023, **2**, 1–11
https://doi.org/10.1093/pnasnexus/pgad289
Advance access publication 5 September 2023
Research Report

Enhanced vibrational stability in glass droplets

Surajit Chakraborty *, Vishnu V. Krishnan [1], Kabir Ramola and Smarajit Karmakar

Tata Institute of Fundamental Research, Hyderabad, 500046 Telangana, India
*To whom correspondence should be addressed: Email: schakraborty@tifrh.res.in
[1]Present address: RCAST, University of Tokyo, 4-6-1 Komaba, Meguro, Tokyo 153-8904, Japan.
Edited By: Krzysztof Żur

Abstract

We show through simulations of amorphous solids prepared in open-boundary conditions that they possess significantly fewer low-frequency vibrational modes compared to their periodic boundary counterparts. Specifically, using measurements of the vibrational density of states, we find that the $D(\omega) \sim \omega^4$ law changes to $D(\omega) \sim \omega^\delta$ with $\delta \approx 5$ in two dimensions and $\delta \approx 4.5$ in three dimensions. Crucially, this enhanced stability is achieved when utilizing slow annealing protocols to generate solid configurations. We perform an anharmonic analysis of the minima corresponding to the lowest frequency modes in such open-boundary systems and discuss their correlation with the density of states. A study of various system sizes further reveals that small systems display a higher degree of localization in vibrations. Lastly, we confine open-boundary solids in order to introduce macroscopic stresses in the system, which are absent in the unconfined system and find that the $D(\omega) \sim \omega^4$ behavior is recovered.

Keywords: amorphous solids, open boundary, vibrational properties, localized modes

Significance Statement

Glasses have long been known to display anomalous dynamical properties, originating from a complex energy landscape that also determines their stability. Much of the research into its origin utilizes computational analysis of their vibrational density of states. Such studies have so far simulated systems with periodic boundary conditions which introduce artificial macroscopic stresses into the system. Our study shows that glasses prepared in open-boundary conditions, which faithfully capture the isolated nature of real amorphous solids, are significantly more stable as compared to their confined counterparts. We find that reduced macroscopic stresses, as well as slow annealing, contribute to this surprising enhanced stability. This sheds new light on the nature of the energy landscape of glasses and real amorphous solids.

Introduction

In contrast to crystalline solids, whose vibrational states are well described by the Debye model, amorphous solids exhibit anomalous mechanical and thermal properties (1–6). For a system in d dimensions, the Debye model predicts a vibrational density of states (VDoS), $D(\omega) \sim \omega^{d-1}$ arising from phonons (7). On the other hand, disordered and anharmonic systems possess an excess of low-frequency modes above the Debye prediction, termed the "Boson peak" (8–11). It has been suggested that the large specific heat of glasses and the plastic failure of amorphous solids are intimately related to these low-frequency nonphononic vibrational modes (12–16). However, a complete understanding of the structural and statistical properties of these vibrational modes has been elusive and remains an important current topic of interest in the field of disordered solids.

Several theoretical frameworks for the vibrations in disordered systems seek to model amorphous solids as an ensemble of anharmonic oscillators. Such a treatment is motivated by a disordered arrangement of particles containing local "soft spots" where the stiffness associated with a collective vibration is very small. The phenomenological "soft potential model" (SPM) treats these regions as noninteracting oscillators and predicts a VDoS $D(\omega) \sim \omega^4$ for the lowest frequencies of stable inherent structures (17–19). An extension to the SPM that includes effects of interactions between the anharmonic oscillators continues to retain the ω^4 behavior of the VDoS (20–22). Other recent theoretical studies also predict a $D(\omega) \sim \omega^4$ at the lowest frequencies (23–25). "Fluctuating Elasticity Theory" on the other hand predicts a low-frequency regime composed of extended modes that scale as $D(\omega) \sim \omega^{d+1}$ in d dimensions (26, 27). More recent work suggests nonaffine displacements as the source of such non-Debye behavior (28, 29). Certain mean field theories such as the "Perceptron Model" (30) and the "Effective Medium Theory" (31) predict nonphononic vibrations with a $D(\omega) \sim \omega^2$ dependence. In this context, numerical investigations of amorphous solids in order to ascertain the nature of the low-lying excitations of such systems are of crucial importance.

Recent numerical studies of amorphous solids have identified a universal $D(\omega) \sim \omega^4$ scaling in the low-frequency regime of the VDoS across a broad class of simulated model systems (32). The

Competing Interest: The authors declare no competing interest.
Received: June 8, 2023. **Accepted:** August 28, 2023

universality of this nonphononic power law at low frequencies has been established in two dimensions (2D), three dimensions (3D), and four dimensions (33–35). In order to extract this behavior, studies have focused on small system sizes, where the lowest frequency quasilocalized vibrations are well separated in energy from the first system-spanning phonon. This suggests that these quasilocalized modes (QLMs) are primarily responsible for the power-law tail in the VDoS (33, 36). Further, suppression of system-spanning vibrations using random pinning protocols has been shown to enhance the nonphononic spectra, thereby displaying a pronounced $D(\omega) \sim \omega^4$ behavior (37). Yet other studies have utilized measures such as participation ratios in order to isolate such QLMs that have been shown to contribute to the observed power-law behavior (38). Simulations of various systems including ultrastable glasses (39), silica models (40), long-ranged models (41), finite-temperature systems (42), and random matrix models (43), all provide significant evidence of the ubiquity of the ω^4 regime of the VDoS. However, other studies simulating amorphous solids report deviations from the universal quartic law. High parent temperatures, poor annealing, and small system sizes have each been shown to result in power-law exponents that are less than 4 (44–46). Recent studies have further identified exponents of 3 and 3.5 in the low-frequency regime (47–49). Confined three-dimensional thin films have also been shown to possess a low-frequency VDoS of ω^3 (50).

A crucial aspect often overlooked in simulations of amorphous solids is the residual shear stresses arising due to periodic boundary conditions (PBC) (51). This implies that energy-minimized configurations of disordered systems under PBC are unstable to shear deformations. It has recently been shown that the low-frequency regime of the VDoS is modified to $D(\omega) \sim \omega^5$ when considering ensembles stable to simple-shear perturbation (52). Significantly, such an increase in the exponent points to a correlation between the shear stability of the system and a reduction in the propensity for localized vibrations. Given these observations, a natural question that arises pertains to the consequences of stabilization against all possible deformations. Solids formed under *open-boundary conditions* (OBC) are a suitable candidate since all elements of their pressure tensor are identically zero for each configuration. Such a state is permitted by a lack of confinement at the boundaries. It is important to note that the OBC system is no longer isotropic and introduces possible radial heterogeneity in structure as well as relaxation dynamics. Furthermore, unlike systems under PBC, phonons in OBC are not required to obey the artificial symmetries enforced by the periodicity. Consequently, solids under OBC can accurately capture features of natural solids, including surface as well as system-size effects.

In this paper, we report a characterization of the VDoS of open-boundary amorphous solids. The low-frequency vibrational properties of open systems remain relatively unexplored (53), and our study forms the first such computational examination of the localized modes of open-boundary amorphous solids. We observe the low-frequency vibrational spectrum of a simulated model amorphous solid under OBC to be of the form $D(\omega) \sim \omega^\delta$ with $\delta > 4$, both in 2D and 3D. Since an increase in the exponent implies a reduction in the degree of vibrational localization, the corresponding solid ensemble may be said to possess enhanced stability. Notably, the model system displays such a VDoS only when configurations are *annealed* to their inherent structures. On the other hand, commonly used quenching protocols lead to ensembles with $\delta \sim 4$. Interestingly, at large enough system sizes, the exponent saturates to a value $\delta = 5$ in 2D and $\delta = 4.5$ in 3D. A detailed investigation of the average stress profile of the solids allows us to identify a surface layer that suggests a source of the system-size effects. Lastly, we also observe that confining open-boundary solids under a harmonic trap recovers the $D(\omega) \sim \omega^4$ behavior of PBC systems, confirming the role of stresses in the stability of solids.

The outline of the paper is as follows. The first section describes the numerical protocol we use to generate stable open-boundary solids. In the second section, we demonstrate the effect of different minimization protocols to generate stable solids. In the third section, we present data to demonstrate the effect of the system size on the vibrational spectrum. In the fourth section, we provide an analysis of the source of the stabilization. In the fifth section, we examine the effect of confinement on the vibrational spectrum of solids. Finally, we conclude and provide directions for future research.

Model and simulation details

In order to simulate the behavior of amorphous solids in OBC, we use models with attractive interactions between the particles. Specifically, we use variants of the canonical Kob–Andersen Lennard–Jones model (54, 55) in 2D and 3D. The model consists of binary mixtures of particles in number ratios 65:35 in 2D and 80:20 in 3D, with an interaction potential:

$$V_{\alpha\beta}(r) = 4\epsilon_{\alpha\beta}\left[\left(\frac{\sigma_{\alpha\beta}}{r}\right)^{12} - \left(\frac{\sigma_{\alpha\beta}}{r}\right)^{6} + \sum_{i=0}^{2} c_{2i}\left(\frac{r}{\sigma_{\alpha\beta}}\right)^{2i}\right], \quad (1)$$

where $\alpha, \beta \in \{A, B\}$ correspond to the two types of particles resulting in three types of interactions. The potential is cut off at a distance $r_c^{\alpha\beta} = 2.5\sigma_{\alpha\beta}$. $\sigma_{AA} = 1$ is the unit of length, and $\epsilon_{AA} = 1$ is the unit of energy (Boltzmann's constant being unity). The remaining parameters are $\epsilon_{AB} = 1.5$, $\epsilon_{BB} = 0.5$, $\sigma_{AB} = 0.8$, and $\sigma_{AB} = 0.88$ with all masses set to unity $m = 1.0$. We equilibrate liquid configurations at high temperatures ($T = 0.55$ in both 2D and 3D) by performing constant temperature molecular dynamics simulations under PBC. The liquid is then cooled to a low temperature ($T = 0.2$) at a rate $\dot{T} = 10^{-4}$. In order to achieve a density close to that of a system under OBC, we perform zero-pressure molecular dynamics simulations using the isobaric ensemble.

Finally, in order to study solid droplets under OBC, we begin by cutting out a circular (spherical in 3D) region of the zero-pressure liquid. We ensure that all the droplet samples contain a fixed number of particles, say N, by selecting the N closest particles to the center of mass of the corresponding liquid sample referred to henceforth as a "cutout" sample. Solids are configurations that resist deformations, which correspond to the inherent structures of the amorphous configuration of particles. We generate such structures by performing an energy minimization of the particle-position degrees of freedom using three different protocols, namely: (i) Molecular dynamics simulations in the presence of dissipative viscous drag in the athermal limit (damped dynamics, DD) (56), (ii) fast inertial relaxation engine (FIRE) (57), and (iii) the nonlinear conjugate gradient (CG) algorithm (58). Note that we do not equilibrate the cutout sample but instead directly quench or anneal through the energy minimization protocol.

Simulations of the largest system-size three-dimensional zero-pressure PBC liquids are performed using LAMMPS (59). The vibrational properties of the solid configurations are probed through the Hessian matrix as defined in Eq. 4. We perform eigenvalue computations using the Intel Math Kernel Library (60) sparse solver routine `mkl_sparse_d_ev`. Below, we discuss the three protocols we employ in order to find the minimum-energy amorphous configurations.

Damped dynamics

In the DD protocol, a dissipative viscous drag in the absence of a temperature bath or other energy input serves as a method to find the stationary state of the conservative force fields. Such an evolution of the system is described by the equation of motion

$$\frac{d\vec{v}_i}{dt} = \vec{F}_i - \gamma \vec{v}_i, \tag{2}$$

where $\vec{F}_i$ is the conservative force on particle i due to interactions with other particles, $\vec{v}_i$ is the instantaneous velocity of the particle i and γ is the viscous damping parameter. A stable steady-state solution of these equations corresponds to a minimum-energy configuration of the system of particles with $\vec{F}_i = 0$ and $\vec{v}_i = 0$ for all particles. We employ a velocity Verlet integration scheme modified to incorporate velocity-dependent accelerations. These damped equations of motion allow the system to traverse the basins of multiple inherent states before selecting and settling in a more stable minimum. We employ small damping constants so that the system is able to execute such a relaxation. At large values of γ, the dynamics would be equivalent to a steepest-descent minimization of the energy. Unless explicitly mentioned the value of the damping constant γ is 0.1.

FIRE minimization

The FIRE is an efficient protocol designed to find local minima of multidimensional functions (57). The procedure involves numerically integrating a dynamical equation with variable viscous damping and, additionally, a gradient director. The equation of motion for each particle is

$$\frac{d\vec{v}}{dt} = \vec{F}(t) - \gamma(t)|v(t)|[\hat{v}(t) - \hat{F}(t)], \tag{3}$$

where $\hat{F}(t)$ refers to unit vector along $\vec{F}(t)$. These two aspects of the FIRE algorithm that lend it its speed also prevent the system from leaving its original energy basin. Therefore, the inherent structure obtained is primarily a function of the equilibrium sampling and is not dependent on the stability of the minimum of the basin.

CG minimization

We also test the stability of configurations obtained via a CG minimization scheme (58). We implement the nonlinear CG for the open boundary system using the Polak-Ribiere method to obtain the updated direction and the secant minimization method in order to determine the step size of the line search. As in the case of the FIRE algorithm, the CG leads the system to its nearest minimum.

Stable vibrational modes

Harmonic vibrations of a solid can be probed by diagonalizing the "Hessian matrix," defined as

$$\mathbf{H}_{ij} \equiv \left.\frac{\partial^2 U(\mathbf{r}_1, \mathbf{r}_2, \ldots \mathbf{r}_n)}{\partial \mathbf{r}_i \partial \mathbf{r}_j}\right|_{\{\mathbf{r}_i^0\}}, \tag{4}$$

where $U(\mathbf{r}_1, \mathbf{r}_2, \ldots \mathbf{r}_n)$ is the total potential energy of the system and $\mathbf{r}_i$ denotes the position of particle i. The eigenvectors (ψ_k) of the Hessian matrix correspond to the cooperative displacements of the particles participating in harmonic vibrations (termed normal modes), and the corresponding eigenvalues (λ_k) represent the frequency of that vibration. The system, when perturbed along a normal mode, will perform a pure oscillation with a frequency $\omega_k = \sqrt{\lambda_k}$. The Hessian matrix evaluated at an energy minimum of the landscape is positive semi-definite with zero modes corresponding to the global invariants of the Hamiltonian (Goldstone modes). For example, a 3D system under PBC possesses three translational degrees of freedom, and the corresponding Hessian, therefore, has three zero modes. Systems under OBC, on the other hand additionally also possess rotational degrees of freedom. In general, in d dimensions, such a solid has $\frac{d(d+1)}{2}$ zero modes corresponding to d translational modes and $\frac{d(d-1)}{2}$ rotational modes. The VDoS of a system of N particles in d dimensions is defined as

$$D(\omega) = \frac{1}{Nd}\sum_{i=1}^{Nd} \delta(\omega - \omega_i). \tag{5}$$

In Fig. 1a and b, we display a typical open-boundary 2D solid configuration of $N = 400$ particles and its first nonzero mode corresponding to a frequency $\omega = 3.24107 \times 10^{-1}$ with a participation ratio (defined in Eq. 16) of 1.313714×10^{-1}. Similarly, in Fig. 1c and d, we show a typical 3D solid of $N = 4,096$ particles and it's first mode corresponding to a frequency $\omega = 4.039514 \times 10^{-1}$ and participation ratio of 6.792794×10^{-3}. These low-frequency modes are quasilocalized with a small number of particles displaying large participation by forming the core of the vibration. Interestingly, these eigenmodes resemble the quadrupolar modes observed in the low-frequency regime of the vibrational density of states of structural glass formers under PBC (32).

Anharmonic stability analysis

While the Hessian characterizes the curvature of the energy minimum and, thereby, the frequency of vibrations, an anharmonic analysis is necessary in order to understand the vicinity of the energy minimum better. The energy near the minimum may be approximated up to the fourth order as

$$\delta U(s) = \frac{1}{2!}B_2 s^2 + \frac{1}{3!}B_3 s^3 + \frac{1}{4!}B_4 s^4, \tag{6}$$

where s is the scalar distance of particles from the minimum along a given direction in the energy landscape. If the particles are displaced along an eigenvector (ψ) of the Hessian (H),

$$B_2 = \psi \cdot H \cdot \psi \tag{7}$$

is the eigenvalue of the Hessian, and

$$B_3 = \psi_i \left[\frac{\partial^3 U}{\partial r_i \partial r_j \partial r_l}\right] \psi_l \psi_j, \tag{8}$$

$$B_4 = \psi_i \psi_l \left[\frac{\partial^4 U}{\partial r_i \partial r_l \partial r_k \partial r_j}\right] \psi_k \psi_j \tag{9}$$

quantify the nonlinearity of the energy landscape along that mode.

Given a vibration in the energy landscape as defined by an eigenvector, the corresponding energy minimum is said to be "stable" provided that the minimum is the deepest in its neighborhood. Under the quartic approximation of the energy near the minimum, such stability is achieved when (18)

$$B_3^2 \leq 3B_2B_4. \tag{10}$$

Effect of minimization protocol

Simulated models studying the properties of amorphous solids have typically been systems under periodic boundaries. It has

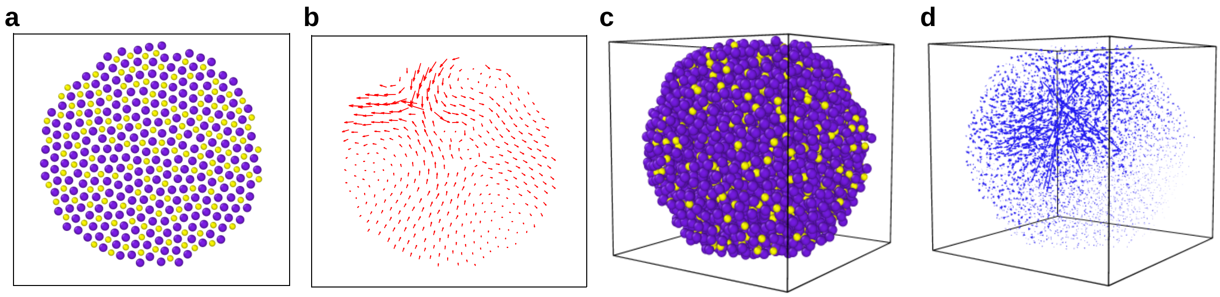

Fig. 1. a) A two-dimensional solid generated from a 400 particle, circular "cutout" of a liquid configuration, via damped dynamics (DD) minimization under OBC. b) The first nonzero vibrational mode of the two-dimensional solid with a participation ratio of approximately 0.26 and a frequency $\omega \approx 4.34 \times 10^{-1}$, displaying typical quasilocalized characteristics. c) A three-dimensional solid configuration of 4, 096 particles under OBC generated using DD energy minimization. d) The first nonzero vibrational mode of the three-dimensional solid with a participation ratio of 0.0068 and a frequency $\omega \approx 4.04 \times 10^{-1}$. Note that the solid borders of the figures are to aid depth perception, especially in 3D. The systems themselves have no boundaries.

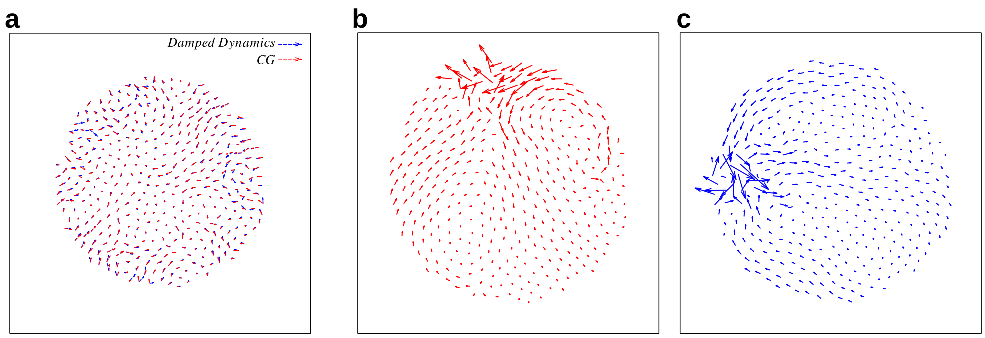

Fig. 2. a) Displacements incurred by each particle from the same liquid configuration when undergoing energy minimization through two different protocols, namely CG and DD. The eigenvectors corresponding to the lowest frequency vibrational modes of the solid configuration obtained via b) CG and c) DD minimization protocols. Under a quartic Taylor expansion of the landscape along the modes, the energy-minimized configuration achieved via b) CG is unstable and by c) DD is stable.

been shown that in such systems, the CG minimization protocol generates configurations with stable minima, provided that configurations are obtained from a sufficiently low parent temperature (32). However, the open-boundary configurations obtained by quenching the cutouts of zero-pressure PBC systems contain, among them, some inherent structures at unstable minima. We, therefore, explore an energy-minimization protocol that anneals the system into an ensemble comprised of primarily stable minima.

We find that different energy-minimization protocols drive the system to different minima. In Fig. 2a, we show the displacements incurred by each particle from a particular liquid configuration when undergoing energy minimization through two different protocols, namely DD and CG. While both procedures yield inherent structure configurations, they do not correspond to the *same* minimum. Most significantly, DD finds minima in a relatively expanded region in the energy landscape as compared to CG and FIRE. In Fig. 3a, we present corroborating numerical evidence with particles undergoing relatively larger displacements in the case of DD. In order to qualify this difference, we compute the distance between the cutout liquid configuration and the energy-minimized solid configuration as

$$d_c = \sqrt{\sum_{i=1}^{N} |\vec{r}_i^{\,L} - \vec{r}_i^{\,S}|^2}, \tag{11}$$

where $\vec{r}_i^{\,L}$ and $\vec{r}_i^{\,S}$ represent the position of particle i in the liquid and solid configurations, respectively. In terms of the radial and tangential displacement incurred by particles at different radial distances,

$$d_c^2 = \int_{r=0}^{R} r\, dr(|u_r(r)|^2 + |u_\theta(r)|^2), \tag{12}$$

where $u_r(r)$ and $u_\theta(r)$ are the radial and tangential displacement of particles at a radial distance r from the center of mass of the liquid droplet. In Fig. 3, we show the average (b) radial and (c) tangential displacement at different radial distances of the liquid configurations. For the case of DD minimization, particles near the surface undergo comparatively larger displacement in the tangential direction, which results in a stable inherent structure. Since the viscosity of the surrounding medium determines the exact extent of this search space, we use an appropriately chosen damping, optimizing for both improved search area as well as speed.

We now consider the vibrational properties of the minima obtained through the various energy minimization protocols. In Fig. 2, we show the lowest frequency vibrational mode of a solid configuration obtained via (b) CG and (c) DD minimization of the same liquid configuration. Although both modes show signatures of similar quadrupolar vibrations, the inherent structure corresponding to (a) does not satisfy the stability criterion defined in Eq. 10.

An important difference between the ensembles of minima obtained via the various protocols lies in their vibrational stability as defined in Eq. 10. Through Fig. 4, we assess the stability of each of the open-boundary solid configurations across the different minimization protocols. We use the quartic Taylor expansion as illustrated in Eq. 6 along the direction specified by the lowest

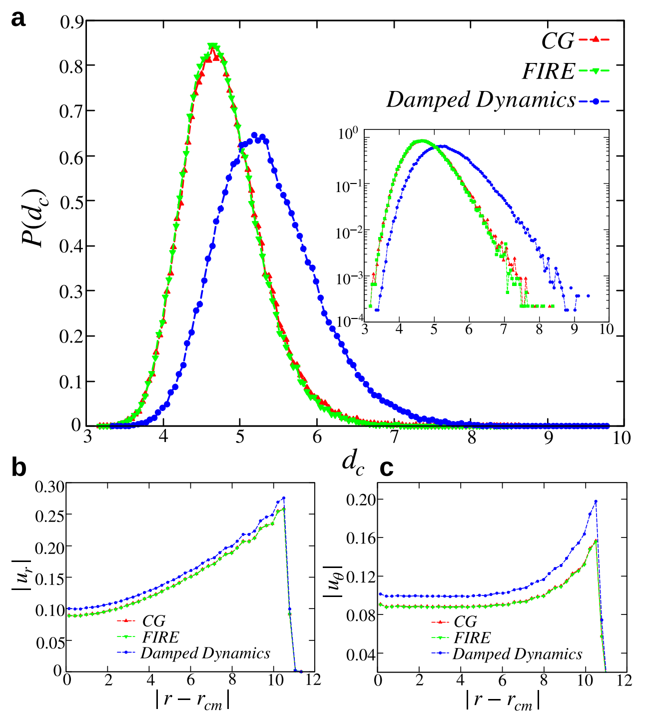

Fig. 3. a) Distribution of the distances between the open-boundary liquid and solid configurations for different minimization protocols. Particles in configurations that underwent DD minimization show relatively larger displacements. (Inset) The distribution plotted in log-scale to highlight the difference at large d_c. Average b) radial and c) tangential displacements incurred by particles at different radial distances. DD produces a large displacement of the particles in the tangential direction, further enhanced near the surface of the liquid as compared to other minimization protocols.

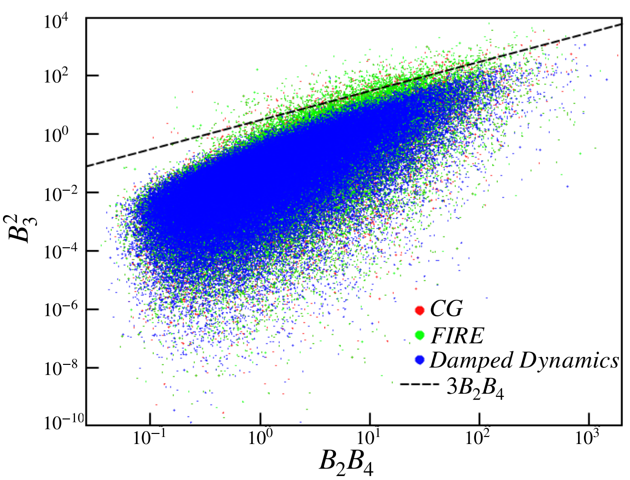

Fig. 4. Scatter plot of B_3^2 against B_2B_4 with a sample size of 2×10^5 solid configurations. The dashed line corresponds to $B_3^2 = 3B_2B_4$ with the region of stability lying below. CG and FIRE minimization protocols produce some inherent structures at unstable minima, whereas DD primarily generate stable minima.

frequency mode in order to extract the stability of the minimum. Interestingly, the CG and FIRE minimization protocols present many unstable inherent structures indicated by the data points above the stability line corresponding to ($B_3^2 = 3B_2B_4$). At the same time, the DD minimizer produces predominantly stable inherent structures as shown by the data points being well within the regime of stability. This suggests that the DD minimizer allows the system to find a locally deeper minimum.

Since the choice of minimization protocol affects the stability of minima, we next examine its effects on the vibrational spectrum. In Fig. 5, we plot the distribution of the low-lying vibrational frequencies of two-dimensional solid ensembles. While the VDoS of CG and FIRE minimized ensembles display the erstwhile universal low-frequency power law $D(\omega) \sim \omega^4$ (32, 34), ensembles generated via the DD minimizer show a power law of ω^5 in the low-frequency regime, as has been seen previously in shear-stabilized systems (52). Generically the smaller the lowest frequency mode, the closer the system is to instability. An increase in the power of the VDoS from 4 to 5 corresponds to a reduction in the proportion of such small-valued modes. Therefore, such a change is a signature of a transformation to a more stable solid ensemble enabled by an appropriate choice of an annealing energy minimizer.

In the inset of Fig. 5, we plot the distribution of

$$\beta = \frac{B_3}{\sqrt{3B_2B_4}}, \tag{13}$$

where states within the dashed lines ($|\beta| < 1$) correspond to stable minima. We find that the stability condition is best satisfied by configurations obtained via DD minimization. Thus, we observe that the model system, under OBC, displays a correlation between stable minima and the vibrational stabilization of the corresponding solid ensembles.

System size effects

It is well known that the low-frequency vibrational spectrum of amorphous solids contains system-spanning phonons in addition to localized vibrations (32). The long-wavelength phonons in a solid with linear dimension L, under PBC, possess a frequency that varies with system size as L^{-1}. This decrease in the frequency of the phonons with increasing system size leads to difficulty in the characterization of quasilocalization at low frequencies. At the same time, the regime of the VDoS that is most amenable to the study of quasilocalized behavior are the frequencies below the first phonon (61). As the phonon frequencies become comparable to the frequencies of QLMs at larger system sizes, it is then necessary to perform a disorder averaging over an increasingly large number of samples in order to distinguish these modes. This becomes computationally infeasible at very large system sizes. Additionally, QLMs also display finite-size effects when the extent of these modes becomes comparable to the size of the system (44). The softness of QLMs, therefore, becomes independent of system size once it surpasses the length scale of the localized vibration. In this context, very small system sizes have been shown to possess an excess of quasilocalized vibrations with $D(\omega) \sim \omega^\delta$ where $\delta < 4$ (44–46), as the finite-size effects dominate in such situations.

Solids prepared under OBC can display additional surface effects in their low-frequency vibrational spectrum, as boundary effects not present in PBC systems also play a role. The stiffness of particle motion near the surface of the solid is small compared to the bulk of the material. Therefore, the eigenmodes are softer near the boundary of the solid. It is thus natural to expect that in small open-boundary solids, there will be stronger surface effects than in larger solids. This occurs in addition to the finite-size effects arising from the interplay between the size of the system and the size of the QLMs. It is therefore important to study the variation of the VDoS with system size under OBC in order to identify regimes of validity of the enhanced stability.

A quantitative characterization of the surface effects may be performed through a measurement of the stress distribution within

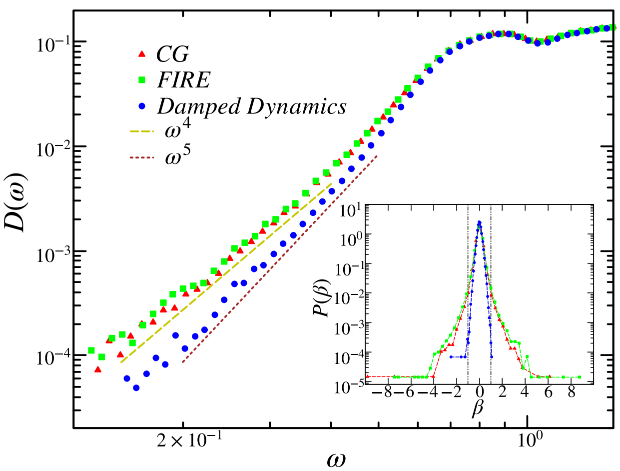

Fig. 5. Distribution of the low-frequency vibrational modes of a 400-particle system in 2D under OBC. The histogram is generated by sampling the first 100 nonzero eigenvalues of 3×10^5 configurations. The solid ensembles generated using CG and FIRE minimizers display a low-frequency behavior of ω^4, whereas using the DD minimizer displays ω^5. (Inset) Distribution of the stability factor $\beta = B_3/\sqrt{3B_2B_4}$ for solids obtained via the various minimization protocols. The dashed vertical lines correspond to $|\beta| = 1$, with the enclosed regions containing stable configurations.

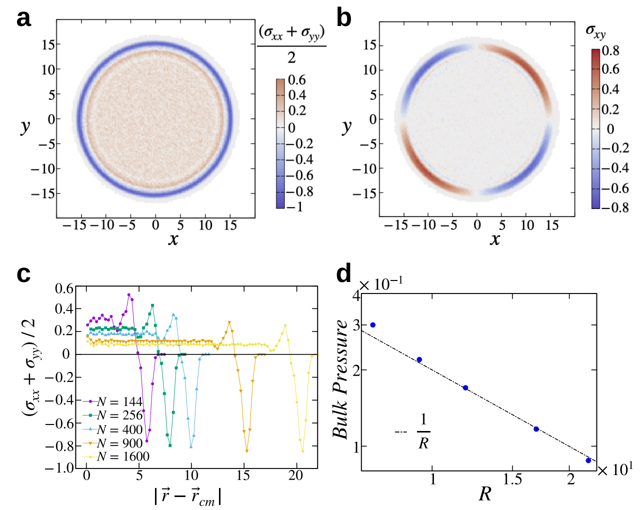

Fig. 6. Spatial distribution of the a) pressure and b) shear stress in solids of system size $N = 900$. The stress profile is constructed by coarse-graining over bins of dimension $0.28\ \sigma_{AA} \times 0.28\ \sigma_{AA}$ and averaging over 10^5 solid configurations. c) Radial distribution of pressure at different system sizes. Boundary layers approximately five particles thick are observed in all systems, independent of size. d) Bulk pressure as a function of system radius. We observe a $\frac{1}{R}$ scaling of the bulk pressure where R is the radius of the solid droplet.

such solids. Moreover, since the low-lying VDoS is crucially sensitive to the macroscopic stress in the amorphous structure (52), it is reasonable to assume that the finite-size effects displayed by the stress profiles also carry over to the VDoS. In PBC systems, the average stress displays homogeneity over the sample, and therefore the local elastic behavior is also independent of the location in the solid. However, as the macroscopic stress is precisely zero in open-boundary solids, any bulk stress is necessarily counterbalanced by the stresses on a "boundary layer." Such a distinct surface region possessing a typical thickness is yet another source of finite-size effects. Additionally, the local elasticity properties of the material are correlated with the local stress distribution, with particles near the boundary displaying lower stiffness in their interaction. In this context, we study the boundary stress layer in solids prepared under OBC, in order to systematically analyze the finite-size effects present in their low-frequency VDoS.

Stress distribution and the boundary layer

In Fig. 6, we describe the stress distributions which highlight the existence of a surface layer in an open-boundary solid. Specifically, in Fig. 6a and b, we plot the spatial distributions of the pressure and shear stress, respectively, as seen in open-boundary solids comprised of 900 particles. These stress profiles are constructed by averaging over 10^5 amorphous configurations and using coarse-graining boxes each of dimension $0.28\ \sigma_{AA} \times 0.28\ \sigma_{AA}$. The typical radius of a configuration is approximately $15\ \sigma_{AA}$ resulting in about 9,000 bins. Figure 6c plots the radial distribution of the pressure for amorphous solids of various sizes. The stress distributions display clear indications of a boundary layer, with the effects of the surface spanning over approximately $5\ \sigma_{AA}$. We also find that while the pressure in bulk is sensitive to the total size of the droplet, the thickness of the boundary layer is largely independent of the system size.

The microscopic stress field ($\sigma_{ij}(\mathbf{r})$) can be expressed as

$$\sigma_{ij}(\mathbf{r}) = \sigma^0_{ij}(\mathbf{r}) + \delta\sigma_{ij}(\mathbf{r}), \tag{14}$$

where $\sigma^0_{ij}(\mathbf{r})$ represents the stress tensor of the initial liquid configuration and $\delta\sigma_{ij}(\mathbf{r})$ is the change in the stress tensor which results from the process of energy minimization. The original distribution of stress σ^0_{ij} in the liquid is dependent on the preparation protocol. The effect of removing a circular cutout from the zero-pressure liquid configuration gives rise to a nontrivial stress distribution near the boundaries of the cutout. This excess stress causes the particles near the edges to be displaced further inwards (due to the attractive nature of the interaction) near the boundaries. This leads to a new stress-balanced state,

$$\partial_i\sigma_{ij}(\mathbf{r}) = 0, \tag{15}$$

with $\delta\sigma_{ij}$ displaying larger changes near the boundary. The condition of mechanical equilibrium at the boundary of the solids is satisfied when the normal force acting on the surface due to the internal pressure exactly balances the surface tension force. Our numerical observations suggest that the stress profile within the surface layer is largely independent of the system size, leading to a constant surface tension across different system sizes. This suggests the bulk pressure will decrease as the radius of the solid is increased. In Fig. 6d, we plot the bulk pressure for different system-size solids. We observe a $P \sim \frac{1}{R}$ scaling of the bulk pressure with the radius of the solid droplet R, which is consistent with a "Laplace law" for the pressure in a droplet (62).

Vibrational density of states

Having characterized the boundary stress layer, we next turn to the system size dependence of the VDoS. We expect the effects of the boundary to be significant only in system sizes for which the width of the boundary is comparable to the radius of the droplet. In order to discern the lengthscales corresponding to such a crossover, we analyze solids of various system sizes with particle numbers ranging from $N = 144$ to 1600 in 2D and from $N = 216$ to 10,000 in 3D.

In Fig. 7, we report the effect of system size on the low-frequency vibrational spectrum of open-boundary solids in 2D.

The small systems ($N = 144, 256$) display a higher degree of softness in their vibration, as can be seen from their low-frequency behavior of $D(\omega) \sim \omega^{4.5}$. The VDoS of systems with particle numbers equal to and larger than 400 appear to exhibit a low-frequency regime of $D(\omega) \sim \omega^5$. This shows a crossover as the size of the system is increased beyond a length scale, with the low-frequency VDoS showing a significant change in the power law, with the exponent varying from 4.5 to 5 in 2D.

The enhanced stability in the VDoS at large system sizes suggests that QLMs in the bulk result in the power law ω^5, whereas modes localized on the surface are much softer and more unstable. We show further analysis comparing bulk and boundary localization in the next section. Finally, such behavior in the thermodynamic limit of the OBC systems under consideration is consistent with earlier studies in PBC systems (52).

In Fig. 8, we plot the VDoS for different system sizes in 3D. Here we observe a low-frequency behavior of $D(\omega) \sim \omega^{4.5}$ in contrast to the results in 2D. In the next section, we perform further analyses to examine this behavior. Moreover, as may be seen in the inset of Fig. 8, we further confirm the robustness of this result by examining the VDoS of solids generated at a much higher degree of annealing by utilizing a damping constant that is one order of magnitude smaller ($\gamma = 0.01$).

Eigenmode localization—surface vs bulk

In this section, we provide further analysis of the lowest frequency vibrational modes in 2D in order to determine the potential source of the stable vibrations achieved under OBC.

The spatial extent of a mode may be evaluated by measuring the participation ratio (PR),

$$\mathrm{PR} = \frac{\left(\sum_{i=1}^{N} \langle \psi_i \mid \psi_i \rangle\right)^2}{N \sum_{i=1}^{N} \left(\langle \psi_i \mid \psi_i \rangle\right)^2}, \tag{16}$$

where $|\psi_i^k\rangle$ denotes the d-dimensional component of the eigenmode ψ^k, corresponding to particle i. System-spanning modes possess a PR close to unity, while spatially localized modes display a PR $\sim 1/N$.

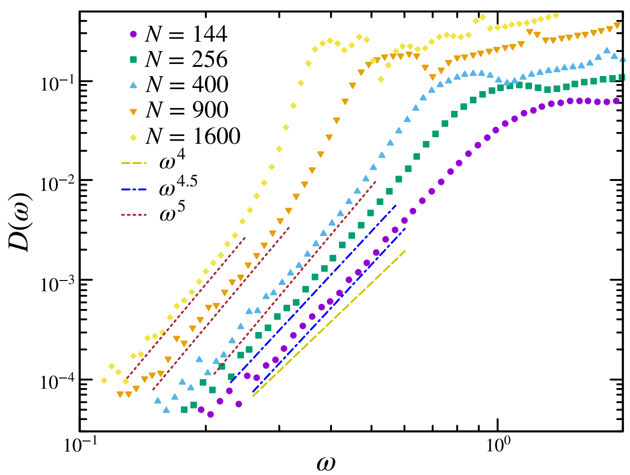

Fig. 7. System size dependence of the low-frequency vibrational spectrum of open-boundary solids in 2D. We have sampled the first 100 nonzero eigenvalues of 2×10^5 configurations for system sizes $N = 144$ and 256. The histograms for the larger system sizes are constructed using 5×10^5 configurations. At small system sizes, the surface effects are more pronounced leading to more soft modes in their vibrational spectrum. They display a $D(\omega) \sim \omega^\delta$ with $\delta < 5$ in the low-frequency regime. Such effects are reduced upon increasing the size with large systems displaying a $D(\omega) \sim \omega^5$.

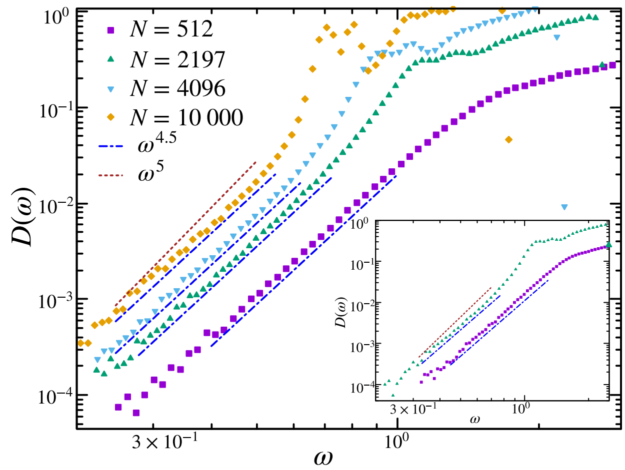

Fig. 8. System size dependence of the low-frequency vibrational spectrum of three-dimensional open boundary solids generated by annealing ($\gamma = 0.1$). We sample the first 100 nonzero eigenvalues of 2×10^5 configurations for system sizes $N = 512$, 2,197, and 4, 096. For the larger system of size $N = 10{,}000$, the histogram is generated by sampling 8×10^4 configurations. (Inset) Distribution of low-frequency modes of various system sizes of three-dimensional solids generated via much slower annealing ($\gamma = 0.01$). These distributions are drawn by sampling the first 100 low-frequency modes of at least 80,000 configurations for each system size. Solids corresponding to all the system sizes and degrees of annealing studied display a $D(\omega) \sim \omega^{4.5}$ in the low-frequency regime of their VDoS.

The contribution of the particles on the surface of the solid to a particular mode may then be estimated through the “Surface Participation” (SP) as defined below:

$$\psi_S^2(k) = \sum_{i \in \texttt{surface}} \langle \psi_i^k \mid \psi_i^k \rangle. \tag{17}$$

The `surface` is defined as encompassing all the particles belonging to the boundary layer as determined by the stress analysis described in the previous section. Modes localized on the surface of the solid display an SP close to 1, whereas a vibration that is localized deeper within the bulk of the solid incurs an SP closer to 0. In Fig. 9a, we plot the probability distribution of SP for the lowest frequency modes in two-dimensional solids of system size $N = 400$. The peak of the distribution corresponds to modes with extended, system-spanning vibrations that all particles participate in. By observation, we consider modes with an SP ≤ 0.7 to be predominantly bulk-localized vibrations and modes with an SP ≥ 0.8 to be predominantly surface-localized. In Fig. 9b and c, we plot histograms of the lowest frequency divided by ω_{min}^δ in order to extract the power law. We find that bulk-localized modes (Fig. 9b) display the stabilized $\delta \approx 5$ while the surface-localized modes (Fig. 9c) present a more unstable $\delta \approx 4.5$. This points to the possibility that the low-stress environment of the bulk contributes stable vibrations, while the large stresses at the surface result in modes of lower stability. Furthermore, such a separation potentially explains the large degree of softness observed in the vibrational spectrum at small system sizes.

We now provide a characterization of the lowest frequency vibrational modes in three-dimensional open-boundary solids. We study the contribution of surface particles on these modes through their “surface participation” (SP) as defined in Eq. 17. In Fig. 10a, we plot the probability distribution of SP corresponding to the lowest frequency modes in three-dimensional solids of various system sizes. The modes with a value of SP corresponding to

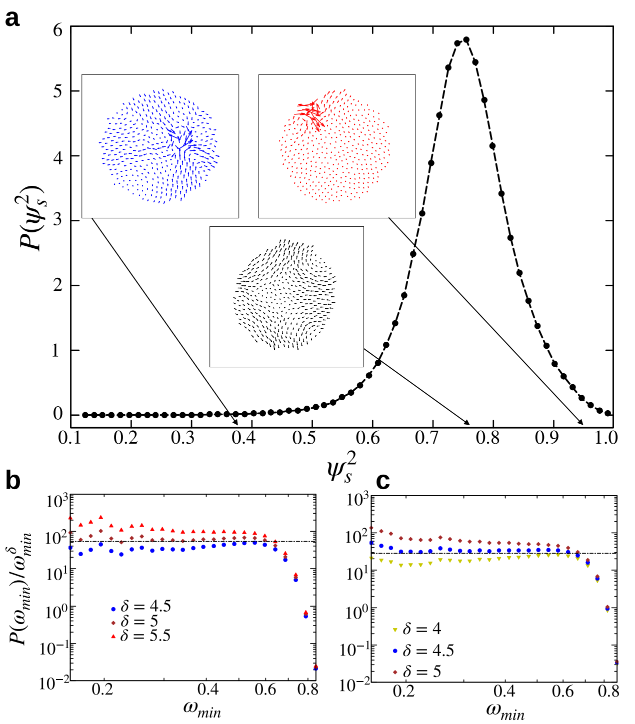

Fig. 9. a) Distribution of "Surface Participation" (SP) for the lowest frequency modes in two-dimensional solids of system size $N = 400$. Modes localized on the surface of the solid display an SP of 1, whereas when SP = 0, the vibration is limited to the inner bulk. The peak of the distribution corresponds to extended modes spanning the whole solid. The distribution of the lowest frequency modes with predominantly b) bulk and c) surface localizations. Here, modes corresponding to an SP ≤ 0.7 are considered to be bulk-localized vibrations and modes with an SP ≥ 0.8 are considered surface-localized vibrations. Both histograms are constructed using 10^5 lowest frequency modes. The bulk-localized modes display a $\delta = 5$, whereas surface-localized modes show a $\delta = 4.5$.

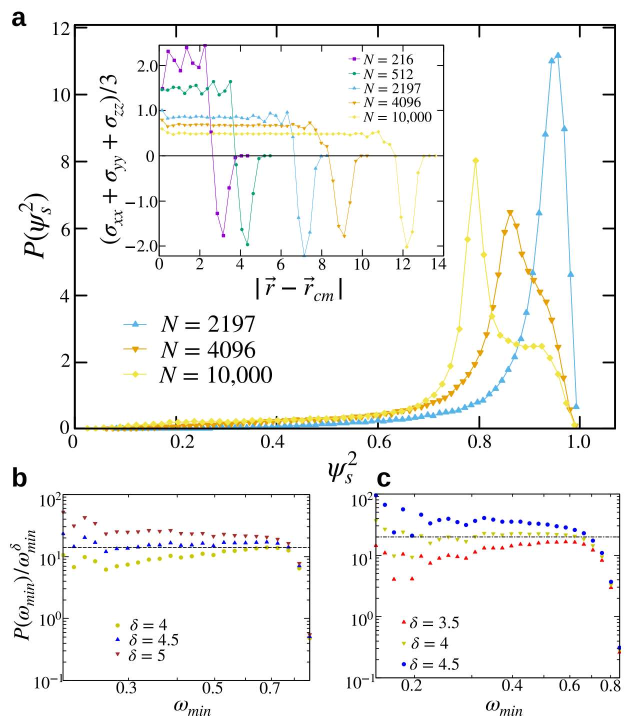

Fig. 10. a) Distribution of SP for the lowest frequency modes in three-dimensional solids of system sizes $N = 2,197$, 4, 096, and 10,000. (Inset) Radial distribution of pressure for three-dimensional solids of various system sizes. In b) and c), we plot $P(\omega_{\mathrm{min}})$ divided by $\omega^{\delta}_{\mathrm{min}}$ for bulk and surface localized modes, respectively. Modes corresponding to SP ≤ 0.82 are considered bulk-localized vibrations, and modes with SP ≥ 0.9 are considered to be surface-localized. Both histograms are constructed using samples of the lowest frequency modes from 5×10^4 configurations. Bulk-localized modes display a $\delta \approx 4.5$, whereas surface-dominated modes show $\delta \approx 4$.

the peaks of the distributions are extended, system-spanning vibrations. In the case of the distribution corresponding to a system size $N = 4,096$, we define the modes with SP ≤ 0.82 as being predominantly bulk-localized vibrations and modes with ≥ 0.9 as predominantly surface-localized. In Fig. 10b and c, we plot histograms of the lowest frequency for bulk and surface-localized modes, respectively. We find that bulk-localized modes display a $\delta \approx 4.5$ and surface-localized modes show a $\delta \approx 4$.

Effect of confining stresses

In this section, we show that the vibrational properties of systems under periodic boundaries can by reproduced by imposing macroscopic stresses on open-boundary solids.

The stresses in a system are described through the force moment tensor, defined as

$$\Sigma_{\alpha\beta} = \sum_{i}\sum_{j} f^{ij}_{\alpha} r^{ij}_{\beta} = \sigma_{\alpha\beta} A, \tag{18}$$

where f^{ij}_{α} is the α-component of the force on particle i by particle j, r^{ij}_{β} is the β-component of the vector distance between the particles i and j, $\sigma_{\alpha\beta}$ is the macroscopic stress tensor and A is the area of the two-dimensional system. Solids prepared under OBC have precisely zero macroscopic stresses, i.e. $\sigma_{xx} = \sigma_{yy} = \sigma_{xy} = 0$. As described in the previous sections, such systems display a $D(\omega) \sim \omega^{\delta}$ with $\delta > 4$, in contrast to PBC systems where $\delta = 4$. It is, therefore, interesting to analyze the effects of re-introducing stresses on the vibrational spectrum of solids.

In order to accomplish this, we have studied the vibrational modes of solids confined in a radially symmetric harmonic trap centered at the center of mass (CM) of the system, as follows:

$$U(\mathbf{r}_1, \mathbf{r}_2, \ldots \mathbf{r}_n) = V(\mathbf{r}_1, \mathbf{r}_2, \ldots \mathbf{r}_n) + \frac{1}{2}\sum_{i=1}^{N} \kappa |\mathbf{r}_i - \mathbf{r}_{CM}|^2, \tag{19}$$

where κ is the spring constant of the trap, $\mathbf{r}_{CM}$ is the location of the CM and $V(\mathbf{r}_1, \mathbf{r}_2, \ldots \mathbf{r}_n)$ represents the pair-wise particle interaction. We then perform DD to obtain energy-minimized solid configurations. Since the center of the harmonic trap is fixed, it breaks translational symmetry. However, it being radially symmetric, the system retains one zero mode corresponding to global rotations. The translational zero modes are substituted with eigenvalues corresponding to the stiffness of the confining harmonic potential. We, therefore, sample the low-frequency modes while excluding the zero modes as well as this trivial addition to the spectrum. In Fig. 11, we display the effect of confinement on the low-frequency vibrational spectrum at various strengths of the harmonic trap. Remarkably, we find that confinement results in a higher degree of softness in the vibrational spectrum of the solids. Increasing the stiffness constant results in large shear stresses in the solid ensemble with a corresponding change in the VDoS from $D(\omega) \sim \omega^5$ to $D(\omega) \sim \omega^4$.

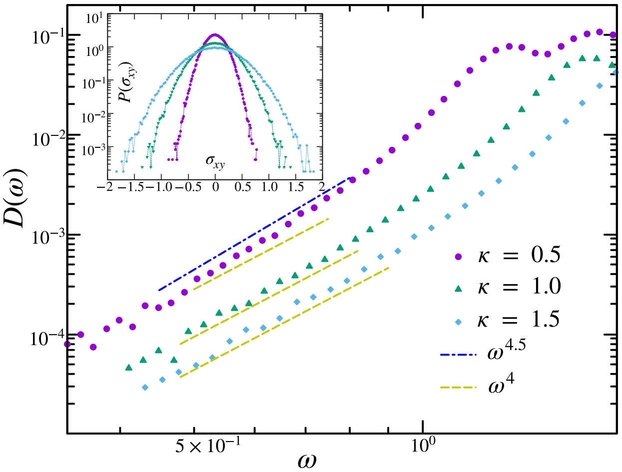

Fig. 11. Effect of confinement on the vibrational spectrum of two-dimensional solids of system size $N = 900$. We have sampled eigenvalues of 10^5 configurations for different stiffness constants. (Inset) Shows the sample-to-sample distribution of shear stress of the solids for different stiffness of the harmonic interaction. Area A of the confined solids is chosen from the radial stress distribution of the solids. Increasing the stiffness constant results in large shear stress fluctuation on the solid ensemble, which changes the VDoS from $D(\omega) \sim \omega^5$ to $D(\omega) \sim \omega^4$ in the low-frequency regime of the solids.

Conclusion and discussion

In this paper, we have performed a detailed characterization of the vibrational modes of amorphous solids prepared under OBC in both 2D and 3D. We showed that structures prepared under OBC differ crucially in their stability properties in comparison to solids prepared with PBC. Specifically, we observed that the $D(\omega) \sim \omega^\delta$ with $\delta = 4$ seen in systems under PBC is modified to a $\delta \approx 5$ in 2D and $\delta \approx 4.5$ in 3D, for solids under OBC. This points to the fact that open-boundary solids which lack any macroscopic stresses are inherently *more stable* than their periodic boundary counterparts. These results reinforce the phenomenon observed by Krishnan et al. (52) where shear-stabilized ($\sigma_{\alpha\beta} = 0\ \forall \alpha \neq \beta$) configurations under PBC display an increase in the exponent to $\delta \approx 5$. Further, we probed the nature of energy minima of systems under OBC through an analysis of the anharmonic coefficients associated with their lowest frequency vibrational mode. Surprisingly we have found that the anharmonic stability of the minimum is sensitive to the protocols employed in generating solid configurations. Moreover, the nature of the minima under consideration is also correlated with a change in the exponent of the VDoS. Specifically, the ensembles with unstable minima correspond to a $D(\omega) \sim \omega^4$, whereas ensembles with stable minima show larger exponents. In particular, we observed clear enhancements in the stability of configurations resulting from dissipative dynamical processes that *anneal* the system when compared to those obtained via quenching minimization protocols. Next, we also characterized the dependence of the low-frequency modes on the system size. Solids at small systems sizes show a higher degree of softness in their low-frequency vibrations, as evidenced by a decrease in the exponent of the VDoS. We also performed an analysis of eigenmode localizations on the boundary and bulk of the system in order to decipher the source of the enhanced stabilization in systems under OBC. We found strong indications that the bulk of the solid predominantly contains stable vibrations, whereas the surface supports unstable modes. Finally, in order to isolate the cause of instability under PBC, we studied the vibrational spectrum of confined solids using a harmonic trap that introduces finite macroscopic stresses in the solid. We indeed showed that the $D(\omega) \sim \omega^4$ behavior of the VDoS is recovered with an increase in the strength of the confinement. This is consistent with recent work where it has been shown that an increasing strain corresponds to an increase in the propensity for low-frequency modes (63).

Our study highlights aspects of the protocols used to create amorphous structures that have direct consequences on the nature of the sampled energy minima. We showed that various energy-minimization procedures populate qualitatively different minima of the landscape, as has also been observed in previous studies (64, 65). Our work in the context of open-boundary solids sheds light on the sparse nature of stable minima in such realistic systems. These results further raise important questions about the limits of stability that may be achieved through sufficient annealing.

Through our analysis of the stress profiles of solids under OBC, we found that the crossovers between the stable and unstable behaviors of the VDoS are well described by a bulk-boundary decomposition of the solids. The enhanced stability is derived from the low-stress environment of the bulk of the solid supported by constant boundary stress. These results point to the fact that the *frozen-in stresses* are crucial in determining the stability of the amorphous solids as well as their VDoS. It would be interesting to use the characterization of the boundary layer and stress distributions that appear in such confined systems to understand the correlations between the macroscopic stress tensor and the distribution of eigenmodes.

Notably, our ensembles exhibit liquid-like surface tensions, as seen by the conformance of bulk pressures to the Laplace law. This observation bares further examination in order to probe any correlation to the enhanced stability of open-boundary solids. Although our results for the cutout protocol reveal striking properties of vibrations in solids under OBC, it would be intriguing to further characterize this behavior with other preparation protocols, such as by evaporation and deposition, which is of direct experimental relevance. Finally, our results in three-dimensional systems regarding their smaller power-law exponent $D(\omega) \sim \omega^{4.5}$ in comparison to two-dimensional systems is surprising in the context of earlier work displaying a universal ω^5 behavior in shear-stabilized systems under PBC. This points to the possibility that systems in higher dimensions support more localization of vibrations. It would be interesting to explore aspects of this nonuniversality in open-boundary systems.

Acknowledgments

We thank Roshan Maharana, Monoj Adhikari, Deepak Dhar, and Prasad Perlekar for useful discussions.

Funding

S.K. would like to acknowledge support through the Swarna Jayanti Fellowship Grant Nos. DST/SJF/PSA-01/2018-19 and SB/SFJ/2019-20/05. The work of K.R. was partially supported by the SERB-MATRICS grant MTR/2022/000966. This project was funded by intramural funds at TIFR Hyderabad under Project Identification No. RTI 4007 from the Department of Atomic Energy, Government of India.

Author contributions

S.K. and K.R. designed the study. S.C. performed the numerical simulations. All authors contributed to the analysis and writing.

Preprints

A preprint of this article is published at https://doi.org/10.48550/arXiv.2303.07147.

Data availability

The code underlying this article is available on GitHub at https://github.com/csurajit/Open_boundary_Amorphous_VDoS/.

References

1 Argon AS. 1979. Plastic deformation in metallic glasses. *Acta Metall*. 27(1):47–58.
2 Demkowicz MJ, Argon AS. 2005. Liquidlike atomic environments act as plasticity carriers in amorphous silicon. *Phys Rev B*. 72(24):245205.
3 Falk ML, Langer JS. 1998. Dynamics of viscoplastic deformation in amorphous solids. *Phys Rev E*. 57(6):7192–7205.
4 Maloney C, Lemaitre A. 2004. Universal breakdown of elasticity at the onset of material failure. *Phys Rev Lett*. 93(19):195501.
5 Pohl RO, Liu X, Thompson EJ. 2002. Low-temperature thermal conductivity and acoustic attenuation in amorphous solids. *Rev Mod Phys*. 74(4):991–1013.
6 Zeller RC, Pohl RO. 1971. Thermal conductivity and specific heat of noncrystalline solids. *Phys Rev B*. 4(6):2029–2041.
7 Kittel C. 2005. *Introduction to solid state physics*. 6th ed. New York: John Wiley & Sons, Inc.
8 Baggioli M, Zaccone A. 2019. Universal origin of boson peak vibrational anomalies in ordered crystals and in amorphous materials. *Phys Rev Lett*. 122(14):145501.
9 Buchenau U, Nücker N, Dianoux AJ. 1984. Neutron scattering study of the low-frequency vibrations in vitreous silica. *Phys Rev Lett*. 53(24):2316–2319.
10 Inoue K, *et al*. 1991. Low-energy excitations in amorphous polymers. *J Chem Phys*. 95(7):5332–5340.
11 Shintani H, Tanaka H. 2008. Universal link between the boson peak and transverse phonons in glass. *Nat Mater*. 7(11):870–877.
12 Anderson PW, Halperin BI, Varma CM. 1972. Anomalous low-temperature thermal properties of glasses and spin glasses. *Philos Mag*. 25(1):1–9.
13 Chen K, *et al*. 2011. Measurement of correlations between low-frequency vibrational modes and particle rearrangements in quasi-two-dimensional colloidal glasses. *Phys Rev Lett*. 107(10):108301.
14 Manning ML, Liu AJ. 2011. Vibrational modes identify soft spots in a sheared disordered packing. *Phys Rev Lett*. 107(10):108302.
15 Widmer-Cooper A, Perry H, Harrowell P, Reichman DR. 2008. Irreversible reorganization in a supercooled liquid originates from localized soft modes. *Nat Phys*. 4(9):711–715.
16 Xu N, Vitelli V, Liu AJ, Nagel SR. 2010. Anharmonic and quasi-localized vibrations in jammed solids—modes for mechanical failure. *Europhys Lett*. 90(5):56001.
17 Galperin YM, Karpov VG, Kozub VI. 1989. Localized states in glasses. *Adv Phys*. 38(6):669–737.
18 Gurarie V, Chalker JT. 2003. Bosonic excitations in random media. *Phys Rev B*. 68(13):134207.
19 Il'In MA, Karpov VG, Parshin DA. 1987. Parameters of soft atomic potentials in glasses. *Sov J Exp Theor Phys*. 65(1):165.
20 Gurevich VL, Parshin DA, Schober HR. 2003. Anharmonicity, vibrational instability, and the boson peak in glasses. *Phys Rev B*. 67(9):094203.
21 Gurevich VL, Parshin DA, Schober HR. 2005. Pressure dependence of the boson peak in glasses. *Phys Rev B*. 71(1):014209.
22 Parshin DA, Schober HR, Gurevich VL. 2007. Vibrational instability, two-level systems, and the boson peak in glasses. *Phys Rev B*. 76(6):064206.
23 Bouchbinder E, Lerner E, Rainone C, Urbani P, Zamponi F. 2021. Low-frequency vibrational spectrum of mean-field disordered systems. *Phys Rev B*. 103(17):174202.
24 Ikeda H. 2019. Universal non-mean-field scaling in the density of states of amorphous solids. *Phys Rev E*. 99(5):050901.
25 Ji W, Popović M, de Geus TWJ, Lerner E, Wyart M. 2019. Theory for the density of interacting quasilocalized modes in amorphous solids. *Phys Rev E*. 99(2):023003.
26 Marruzzo A, Schirmacher W, Fratalocchi A, Ruocco G. 2013. Heterogeneous shear elasticity of glasses: the origin of the boson peak. *Sci Rep*. 3(1):1–7.
27 Schirmacher W. 2011. Some comments on fluctuating-elasticity and local oscillator models for anomalous vibrational excitations in glasses. *J Non Cryst Solids*. 357(2):518–523.
28 Baggioli M, Zaccone A. 2022. Theory of sound attenuation in amorphous solids from nonaffine motions. *J Phys Condens Matter*. 34(21):215401.
29 Szamel G, Flenner E. 2022. Microscopic analysis of sound attenuation in low-temperature amorphous solids reveals quantitative importance of non-affine effects. *J Chem Phys*. 156(14):144502.
30 Franz S, Parisi G, Urbani P, Zamponi F. 2015. Universal spectrum of normal modes in low-temperature glasses. *Proc Natl Acad Sci USA*. 112(47):14539–14544.
31 DeGiuli E, Lerner E, Brito C, Wyart M. 2014. Force distribution affects vibrational properties in hard-sphere glasses. *Proc Natl Acad Sci USA*. 111(48):17054–17059.
32 Lerner E, Bouchbinder E. 2021. Low-energy quasilocalized excitations in structural glasses. *J Chem Phys*. 155(20):200901.
33 Kapteijns G, Bouchbinder E, Lerner E. 2018. Universal nonphononic density of states in 2D, 3D, and 4D glasses. *Phys Rev Lett*. 121(5):055501.
34 Lerner E, Düring G, Bouchbinder E. 2016. Statistics and properties of low-frequency vibrational modes in structural glasses. *Phys Rev Lett*. 117(3):035501.
35 Richard David, *et al*. 2020. Universality of the nonphononic vibrational spectrum across different classes of computer glasses. *Phys Rev Lett*. 125(8):085502.
36 Paoluzzi M, Angelani L, Parisi G, Ruocco G. 2020. Probing the Debye spectrum in glasses using small system sizes. *Phys Rev Res*. 2(4):043248.
37 Angelani L, Paoluzzi M, Parisi G, Ruocco G. 2018. Probing the non-Debye low-frequency excitations in glasses through random pinning. *Proc Natl Acad Sci USA*. 115(35):8700–8704.
38 Mizuno H, Shiba H, Ikeda A. 2017. Continuum limit of the vibrational properties of amorphous solids. *Proc Natl Acad Sci USA*. 114(46):E9767–E9774.
39 Wang L, et al. 2019. Low-frequency vibrational modes of stable glasses. *Nat Commun*. 10(1):1–7.
40 Bonfanti S, Guerra R, Mondal C, Procaccia I, Zapperi S. 2020. Universal low-frequency vibrational modes in silica glasses. *Phys Rev Lett*. 125(8):085501.
41 Das P, Hentschel H, Lerner E, Procaccia I. 2020. Robustness of density of low-frequency states in amorphous solids. *Phys Rev B*. 102(1):014202.
42 Das P, Procaccia I. 2021. Universal density of low-frequency states in amorphous solids at finite temperatures. *Phys Rev Lett*. 126(8):085502.

43 Stanifer E, Morse PK, Middleton AA, Manning ML. 2018. Simple random matrix model for the vibrational spectrum of structural glasses. *Phys Rev E*. 98(4):042908.
44 Lerner E. 2020. Finite-size effects in the nonphononic density of states in computer glasses. *Phys Rev E*. 101(3):032120.
45 Lerner E, Bouchbinder E. 2017. Effect of instantaneous and continuous quenches on the density of vibrational modes in model glasses. *Phys Rev E*. 96(2):020104.
46 Lerner E, Bouchbinder E. 2022. Nonphononic spectrum of two-dimensional structural glasses. *J Chem Phys*. 157(16):166101.
47 Wang L, Fu L, Nie Y. 2022. Density of states below the first sound mode in 3D glasses. *J Chem Phys*. 157(7):074502.
48 Wang L, Szamel G, Flenner E. 2021. Low-frequency excess vibrational modes in two-dimensional glasses. *Phys Rev Lett*. 127(24): 248001.
49 Wang L, Szamel G, Flenner E. 2023. Scaling of the non-phononic spectrum of two-dimensional glasses. *J Chem Phys*. 158:126101.
50 Yu Y, 2022. The ω^3 scaling of the vibrational density of states in quasi-2D nanoconfined solids. *Nat Commun*. 13(1):3649.
51 Dagois-Bohy S, Tighe BP, Simon J, Henkes S, Van Hecke M. 2012. Soft-sphere packings at finite pressure but unstable to shear. *Phys Rev Lett*. 109(9):095703.
52 Krishnan VV, Ramola K, Karmakar S. 2022. Universal non-Debye low-frequency vibrations in sheared amorphous solids. *Soft Matter*.18:3395–3402.
53 Tanguy A, Wittmer JP, Leonforte F, Barrat J-L. 2002. Continuum limit of amorphous elastic bodies: a finite-size study of low frequency harmonic vibrations. *Phys Rev B*. 66:174205.
54 Brüning R, St-Onge DA, Patterson S, Kob W. 2008. Glass transitions in one-, two-, three-, and four-dimensional binary Lennard–Jones systems. *J Phys Condens Matter*. 21(3):035117.
55 Kob W, Andersen HC. 1995. Testing mode-coupling theory for a supercooled binary Lennard–Jones mixture I: the van Hove correlation function. *Phys Rev E*. 51(5):4626–4641.
56 Mandal R, Bhuyan PJ, Chaudhuri P, Dasgupta C, Rao M. 2020. Extreme active matter at high densities. *Nat Commun*. 11(1):1–8.
57 Bitzek E, Koskinen P, Gähler F, Moseler M, Gumbsch P. 2006. Structural relaxation made simple. *Phys Rev Lett*. 97(17):170201.
58 Shewchuk JR. 1994. An introduction to the conjugate gradient method without the agonizing pain. Pittsburgh, USA.
59 A. P. Thompson, H. M. Aktulga, R. Berger, D. S. Bolintineanu, W. M. Brown, P. S. Crozier, P. J. in 't Veld, A. Kohlmeyer, S. G. Moore, T. D. Nguyen, R. Shan, M. J. Stevens, J. Tranchida, C. Trott, S. J. Plimpton. 2022. LAMMPS - a flexible simulation tool for particle-based materials modeling at the atomic, meso, and continuum scales. *Comp Phys Comm*. 271:10817.
60 Intel. 2021. Math Kernel Library.
61 Gartner L, Lerner E. 2016. Nonlinear modes disentangle glassy and Goldstone modes in structural glasses. *SciPost Phys*. 1(2):016.
62 Behroozi F. 2022. A fresh look at the Young-Laplace equation and its many applications in hydrostatics. *Phys Teach*. 60(5):358–361.
63 Kriuchevskyi I, Sirk TW, Zaccone A. 2022. Predicting plasticity of amorphous solids from instantaneous normal modes. *Phys Rev E*. 105(5):055004.
64 Angelani L, Ruocco G, Sampoli M, Sciortino F. 2003. General features of the energy landscape in Lennard–Jones-like model liquids. *J Chem Phys*. 119(4):2120–2126.
65 Nishikawa Y, Ozawa M, Ikeda A, Chaudhuri P, Berthier L. 2022. Relaxation dynamics in the energy landscape of glass-forming liquids. *Phys Rev X*. 12(2):021001.